Characteristics of the flow around a circular OWC-type wave energy converter supported by a bottom-sitting C-shaped structure

Zhenhua Huang[a,*], Shijie Huang[a], Conghao Xu[b,a]

[a]*Department of Ocean and Resources Engineering, School of Ocean and Earth Science and Technology,University of Hawaii at Manoa, Honolulu HI, 96822, USA*
[b]*Changsha University of Science and Technology, Changsha, Hunan, China*

Abstract

Flow characteristics in the vicinity of bottom-sitting wave energy converters are important for understanding the wave loading on and the local scour around the structure. Based on three-dimensional numerical simulation results, key features of the vortex flow in the vicinity of a circular oscillating water column (OWC) supported by a C-shaped structure are discussed, including vortices shed from the lower tip of the OWC chamber and the two edges of the C-shaped support structure. Numerical results reveal a time-mean flow pattern in the vicinity of the C-shaped structure. There is a strong connection between the near-field flow pattern and the local morphological change at the C-shaped support structure.

Keywords: Regular waves; Vortex; Scour; Mean flow; Wave power; Two-phase flow

1. Introduction

Energy is fundamental for modern life. With the increase of global demand for more electricity over the last decades, there is a rising concern of the environmental consequences of fossil fuel based energy sources, and a rise of the global need for clean and renewable energy over the last decades. For example, as a core strategic goal of its energy policy, the state of Hawaii aims at achieving 100 percent renewable energy generation by 2045 (Hawaii State Energy Office, 2007). Ocean wave energy is one important source of renewable energy in the ocean, with the available ocean wave energy being on the terawatt level (Bureau of Ocean Energy Management, 2017). However, compared to other established renewable energy sources such as hydropower, tidal power, wind power and solar power, electricity generation by wave power is still not a widely employed commercial technology presently. This is mainly because of the low conversion efficiency of existing wave energy converters (WECs), the safety

*Corresponding author contacts:
Email address: zhenhua@hawaii.edu (Zhenhua Huang)

Preprint submitted to Applied Ocean Research *May 12, 2020*

of wave energy devices, and the high initial investment in building wave-energy power plants. The last two factors are related to certain extent. Therefore, more research is needed on the safety of wave energy devices to make electricity generation by wave power economically viable.

The operation principles of existing WECs can be broadly divided into three groups: (1) Oscillating Water Columns (OWCs), which use an air turbine, driven by wave-induced compression and expansion of the air inside a pneumatic chamber, to produce electricity; (2) Wave Activated Bodies (WABs), which uses a hydraulic system, driven by wave-induced oscillation of mechanical members, to generate electricity; (3) Over-topping Devices (OTDs), which use an underwater turbine, driven by a water level difference caused by wave-induced over-topping into a reservoir, to produce electricity. Each type of these WECs has its own pros and cons.

Bottom-sitting OWC-type WECs have the advantages of having the turbine above water surface and less frictional loss caused by oscillatory motions of mechanical members. Deng et al. (2013) proposed an OWC-type WEC, which integrates a circular OWC into a bottom-sitting pile structure; a row of such OWC-type WECs can form a dual functional wave-power plant for shore protection and wave energy extraction (Xu and Huang, 2018).

Most existing studies of WECs have focused on wave energy extraction efficiency. Other aspects such as characteristics of local flow field and the safety analysis of WECs have seldom been found in the literature. Compared to floating OWCs, whose safety is largely associated with the mooring line safety, the safety of a bottom-sitting OWC is affected by the loading on and the wave-induced scour around the structure, both are closely related to the characteristics of local flow field.

Only a limited number of studies on wave loads on WECs have been reported in the literature. Representative studies are: an experimental study of wave forces on a fixed 2-D OWC WEC (Ashlin et al., 2015); an experimental study of wave loading on a point absorber (Jakobsen et al., 2016); a CFD simulation of the wave force on a fixed 2-D rectangular OWC device (Elhanafi, 2016); a numerical simulation of the wave forces on a 3-D floating WEC (Sjkvist et al., 2017); a theoretical analysis of wave force on a 2-D heaving WEC (Tom et al., 2019). More recently, Huang et al. (2019) performed a CFD simulation of the wave loading on a bottom-sitting OWC pile (Deng et al., 2013; Xu et al., 2016; Xu and Huang, 2019).

In addition to wave loading on a bottom-sitting WEC structure, formation of wave-induced scour may weaken the foundation of the WEC structure, potentially compromising the safety of the structure. Near-field hydrodynamic features (flow characteristics) are responsible for the local sediment transport and scour around a bottom-sitting WEC, and are the focus of this study.

There is a rich literature in the near-field hydrodynamic features and the resulting local scour around a vertical pile; however, the existing studies focuses mainly on local scours caused by steady currents for the purpose of foundation safety of bridge piers (see for example, Breusers et al., 1977; Chiew and Melville, 1987; Sheppard et al., 2004). Studies of local scour around a standalone pile exposed to regular waves are scarce and exiting studies (Kobayashi and Oda, 1994; Sumer and Fredsøe, 1997, 1998) are guided largely by the knowledge derived from the literature in current-induced scour. The main hydrodynamic features that are responsible for the current-induced local scour around a vertical pile (see for example, Sumer et al., 1992a; Mattioli et al., 2012; Manes and Brocchini, 2015; Xu et al., 2019) include: (1) horseshoe vortex generated at the toe of the pile; (2) lee-wake vortex at the back of the pile; (3) streamline contraction around the pile structure. The mechanisms of current-induced scour are possibly still valid under oscillatory flows such as regular waves (Sumer et al., 1992b). However, hydrodynamic features under an oscillatory flow differ from those under a steady current (Sumer et al., 1992a), mainly due to the flow reversal in oscillatory flows, which may strongly affect the size and stability of the horse-shoe vortex and lee-wake vortex around a vertical pile exposed to waves.

In this study, air-water two-phase flow simulations are used to simulate interaction of regular waves with a bottom-sitting OWC pile, focusing on key characteristics of near-field flow field that affect local sediment transport, including vortex shedding and mean velocity field. The numerical implementation is achieved by using the open source software package OpenFOAM®. Section 2 describes the governing equations, numerical setup and model verification. Section 3 describes the numerical results of the velocity field in the vicinity of an OWC pile, and Section 4 presents a brief discussion of the present numerical results. Major conclusions are summarized in Section 5.

2. Mathematical model, numerical setup and model verification

An air-water two-phase flow model was used to simulate the interaction between regular waves and a bottom-sitting OWC, which uses an orifice to simulate the power take-off (PTO). The implementation of the two-phase flow model is based on the open-source computational fluid dynamics library OpenFOAM®(Weller et al., 1998). The version used in this study is OpenFOAM V1812 from ESI-OpenCFD. This section describes the mathematical model, numerical setup and validation and verification of the numerical model. The verified model will be used in Section 3 to study the near-field hydrodynamic features responsible for the local sediment transport and scour around a bottom-sitting OWC pile.

2.1. Mathematical model

The air-water two-phase flow model employs in-compressible Reynolds-Averaged Navier-Stokes equations (RANS) for a water-air mixture. The saturation of water in a particular volume is denoted by s: for the air above the air-water surface $s = 0$ and for the water below the air-water surface $s = 1$. The air-water interface is treated as a thin layer of the water-air mixture. In this thin layer, $0 < s < 1$ and the density ρ and the dynamic viscosity μ of the water-air mixture are calculated by

$$\rho = s\rho_w + (1 - s)\rho_a, \tag{1}$$

$$\mu = s\mu_w + (1-s)\mu_a, \tag{2}$$

where the subscripts w and a stand for water and air, respectively.

The water-air interface is tracked by a modified VOF method, which uses the following phase equation governing the saturation of water s

$$\frac{\partial s}{\partial t} + \nabla \cdot [s\mathbf{u}] + \nabla \cdot [\mathbf{u}_r s(1-s)] = 0, \tag{3}$$

where $\mathbf{u}$ is the velocity of the air-water mixture and $\mathbf{u}_r$ is an interface compression velocity to suppress the diffusive behavior (Rusche, 2003).

The continuity equation for the water-air mixture is

$$\nabla \cdot \mathbf{u} = 0, \tag{4}$$

where $\mathbf{u}$ is the velocity field of the water-air mixture. The momentum equation for the air-water mixture is

$$\frac{\partial \rho \mathbf{u}}{\partial t} + \nabla \cdot [\rho \mathbf{u}\mathbf{u}^T] = \rho \mathbf{g} - \nabla p + \nabla \cdot [\mu \nabla \mathbf{u} + \rho \mathbf{T}], \tag{5}$$

where p is the pressure of the air-water mixture, $\mathbf{g}$ is the gravitational acceleration, and $\mathbf{T}$ is the specific Reynolds stress tensor of the air-water mixture and calculated by:

$$\mathbf{T} = \frac{2}{\rho}\mu_t \mathbf{S} - \frac{2}{3}k\mathbf{I}, \tag{6}$$

where k is the turbulent kinetic energy, μ_t the dynamic turbulent eddy viscosity, $\mathbf{I}$ the identity tensor, and $\mathbf{S}$ the strain rate tensor expressed by

$$\mathbf{S} = \frac{1}{2}[\nabla \mathbf{u} + (\nabla \mathbf{u}^T)]. \tag{7}$$

The dynamic turbulent eddy viscosity μ_t is expressed as

$$\mu_t = \rho \frac{k}{\tilde{\omega}}, \tag{8}$$

with

$$\tilde{\omega} = \max\left\{\omega, C_{lim}\sqrt{\frac{2\mathbf{S}:\mathbf{S}}{\beta^*}}\right\}, \tag{9}$$

where ω is a characteristic eddy frequency, and C_{lim} and β^* are model parameters.

The following $k-\omega$ SST turbulence model (Wilcox, 1993) is adopted to obtain the turbulent kinetic energy k and the characteristic eddy frequency ω:

$$\frac{\partial \rho\omega}{\partial t} + \nabla\cdot[\rho\mathbf{u}\omega] = \alpha p_\omega - \beta\rho\omega^2 + \frac{\sigma_d}{\omega}\rho\nabla k\cdot(\nabla\omega)^T + \nabla\cdot\left[\left(\mu+\sigma_\omega\rho\frac{k}{\omega}\right)\nabla\omega\right], \quad (10)$$

and

$$\frac{\partial \rho k}{\partial t} + \nabla\cdot[\rho\mathbf{u}k] = p_k - \beta^*\rho\omega k + \nabla\cdot\left[\left(\mu+\sigma^*\mu_t\right)\nabla k\right], \quad (11)$$

where p_k and p_ω are, respectively, the production terms of k and ω. The following expressions for p_k and p_ω are adopted in order to suppress the abnormal growth of the turbulent viscosity and turbulent kinetic energy across the interface in potential flows (Mayer and Madsen, 2000; Jacobsen et al., 2012):

$$p_k = \mu_t\left(\nabla\times\mathbf{u}\right)\cdot\left(\nabla\times\mathbf{u}\right)^T, p_\omega = \frac{\omega}{k}p_k. \quad (12)$$

The expressions given in Eq.(12) state that the production of turbulent kinetic energy is related to the vorticity of the fluid motion, instead of the shear rate of the fluid velocity. It is noted that expressions given in Eq.(12) are different from the original forms of the turbulence production terms suggested by (Wilcox, 1993, 2008).

We use the following values suggested by Wilcox (2008) for the model parameters in the $k-\omega$ model: $\alpha = 13/25$, $\beta = 0.072$, $\beta^* = 0.09$, $\sigma_\omega = 0.5$, $\sigma^* = 3/5$ and $C_{lim} = 7/8$.

2.2. Boundary conditions

To setup a numerical wave flume based on the mathematical model given in Section 2.1, the following boundary conditions are used: (i) wave inlet boundary conditions at the inlet for wave generation; (ii) wall boundary conditions on the bottom, and two lateral boundaries, and at outlet boundary; (iii) atmospheric boundary condition at the top boundary of the computational domain; and (iv) wall boundary conditions on the surfaces of a physical model. Because the roughness of stainless steel surfaces is usually just a few micrometers, which is much less than the thickness of viscous sub-layer, all wall boundaries are assumed to be hydraulically smooth.

2.3. Numerical setup for an empty wave flume

A three-dimensional numerical wave flume of 24.00 m long and 0.50 m high was used to perform all numerical simulations reported in this study. As shown in Fig. 1, the numerical wave flume consists of two sections: the test section (from x=0.00 m to 10.00 m) and the wave absorbing section (from x=10.00 m to 24.00 m).

The width of the numerical wave flume changes depending on the problem to be simulated. The dimensions of the wave flume are described by a Cartesian coordinate system (x, y, z), with x pointing in the direction of wave propagation, z vertical

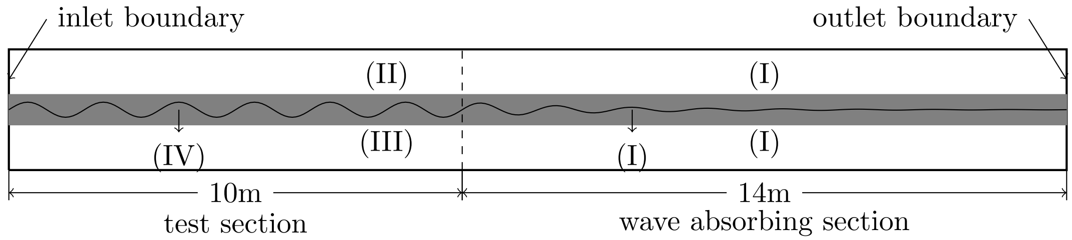

Fig. 1: A sketch of the side view of the numerical wave flume. Not drawn to scale

upward and y in the lateral direction. The origin of this coordinate system is at the inlet boundary where waves are generated. Regular waves are generated by specifying velocity and elevation at $x = 0$ m by using the second order Stokes wave theory (see Section Appendix A for details).

The empty wave flume is divided into four zones: (1) wave absorption zones; (2) air zone; (3) water zone; and (4) near air-water interface zone in which the wave crests and wave troughs lie. Nested grids are used in the computational domain, with each zone having a different grid. The information of the grid for each zone is summarized in Table 1.

Fig. 2 shows comparisons between the theoretical and simulated time series of surface displacements at two locations. In the simulation, the waves are generated using second order Stokes waves at the inlet boundary. The crest and trough given by the second-order Stokes wave theory are also included in the figure for comparison. The spatial attenuation between the two locations, which are 3.5 m apart, is negligible. The simulated crest and trough agree well with the theoretical values (the 1-mm difference in the wave crests at two locations is due to the adjustment of the second-order Stokes waves). At the end of the wave absorption zone, the surface displacement is expected to be zero for an adequate wave absorption zone; Fig. 2 shows that the simulated surface displacement at x =23.5 is virtually zero, suggesting that the wave absorption used in the simulation is adequate. It can be concluded that the model and the numerical setup for the empty wave flume are suitable for simulating generation and propagation of second-order Stokes waves with adequate accuracy. Therefore, when an OWC model is installed in the numerical wave tank, the same numerical setup will be used for wave generation and propagation, except in the vicinity of the OWC model where another set of near-field nested grids are needed to resolve required flow features,

Table 1: Information of the grids for the empty wave flume

size/zone	Zone (I)	Zone (II)	Zone (III)	Zone (IV)
Δx (m)	0.02∼0.12	0.02	0.02	0.02
Δy (m)	0.05	0.05	0.05	0.05
Δz (m)	0.01	0.01	0.01	0.005

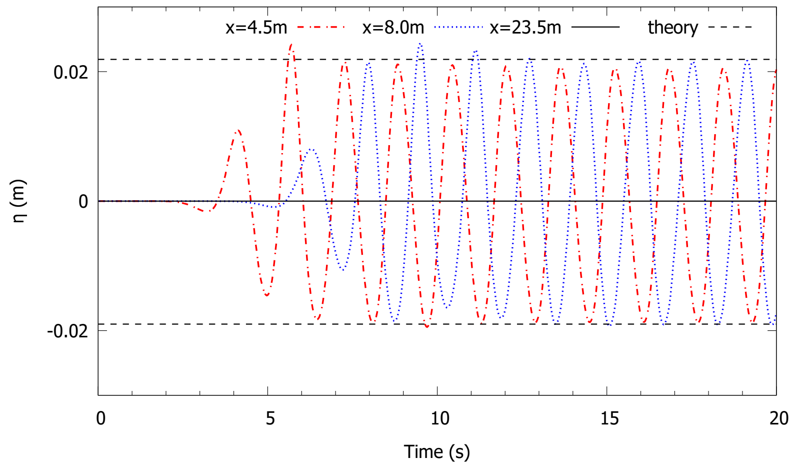

Fig. 2: The simulated and theoretical (2nd order Stokes wave theory) time series of surface displacements at two locations. The dashed lines indicate the crest and trough given by the second order Stokes wave theory.

2.4. Model verification

Lopez et al. (2015) reported a set of measured flow fields inside a 2D breakwater-integrated OWC. The measurement was done using a Particle Image Velocimetry (PIV). The validation and verification of the numerical model is done by comparing the flow fields simulated by the present model with those measured by PIV. The main purpose of the comparison is to make sure that our numerical simulation can capture the main features of the near-field flow field and the vortices shed from the lower tip of the rectangular OWC chamber.

In the experiment of Lopez et al. (2015), the water depth was kept at $d = 0.29$ m, and the incident waves had a wave height of $H = 0.060$ m and a wave period of $T = 1.6$ s. The OWC model geometry and the near-field nested grids for modeling it are shown in Fig. 3. Grids finer than those used for the empty wave flume are needed to accurately simulate the wave-interaction with this OWC model. In particular, appropriate finer grids are needed to simulate the air flow through the orifice and the vortex shedding from the sharp edges of the model. The total number of mesh count used in the simulation is around 1.8 million. For numerical stability, the CFL numbers in the range of 0.4 and 0.6 have been used in the simulations. The bottleneck in this simulation is the high speed air flow through the orifice, which requires small grid size and very small time step. The code was run on a workstation with 18 cores, and about 200 wall-clock hours were needed to produce 20 s of real-time results.

To show that the mathematical model and the numerical setup, especially the grids used to resolve the vortices shed from the sharp edges of the OWC model, are suitable for the problem, the velocity fields measured using a PIV at three selected phase angles within one period are compared with the simulated in Fig. 4. Very good agreements between the measurement and simulation can be observed at these

Figures/sketch-tif-converted-to.png

(a)

Figures/mesh-tif-converted-to.png

(b)

Fig. 3: Left: a 3D view of the rectangular OWC model studied by Lopez et al. (2015); Right: The two nested local grids used to simulate the OWC model

three phase angles[1]. It is remarked that at the phase"g", the simulation shows a counter-rotating vortex underneath the tip of the skirt. This is possibly because much higher spatial resolution is used in the numerical simulation than in the PIV measurement. Lopez et al. (2015) measured the velocity fields at eight phase angles within a period; the agreements between the measured and simulated velocity fields at other five phase angles (not shown here) are also reasonably good. Since the color scheme used to produce the color maps for the vorticity in the experimental results is not available, information on the vorticity is not included in the simulated results. It is concluded that the numerical model and the grids used here are capable of simulating the vortices shed from the vertical thin plate.

3. Results for a bottom-sitting OWC pile

The OWC model considered here is the one experimentally studied by Xu et al. (2016). The left panel of Fig. 5 shows the bottom-sitting OWC-type WEC considered in this study. This bottom-sitting OWC-type WEC consists of two sections: a circular OWC chamber section which is a circular tube section covered on the top by a plate with an orifice and a C-shaped support structure which joins to the lower end of OWC chamber section. The portion of the OWC chamber that is not joined to the C-shaped support structure is the skirt of the OWC chamber. Hereinafter, this bottom-sitting OWC-type WEC is referred to as "a bottom-sitting OWC pile" or "an OWC pile" for short, and the skirt of the OWC chamber is simply referred to as "the skirt" for

[1] Lopez et al. (2015) states that the thickness of the vertical walls in their OWC model is 2.5 cm; but in the figures showing the measured velocity fields the thickness of vertical walls less than 2.5 cm can be observed. The velocity fields from the present numerical simulations are presented using a wall thickness of 2.5 cm, consistent with the dimension stated in Lopez et al. (2015).

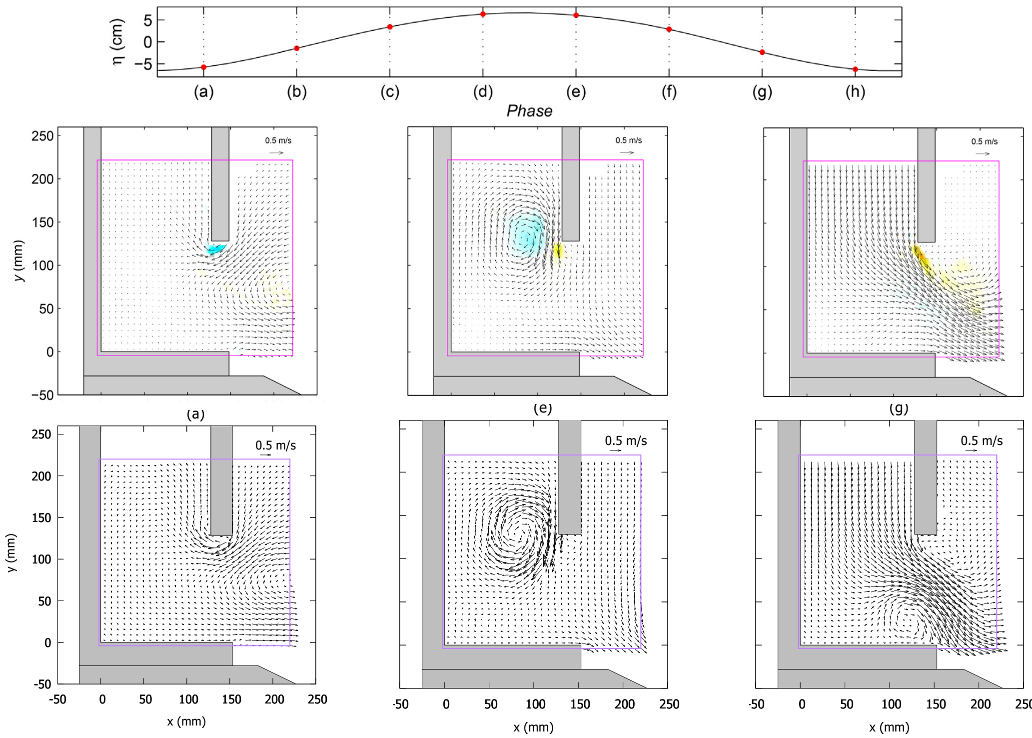

Fig. 4: Comparison of velocity fields between the measured (top row) and simulated (bottom row) velocity fields at three selected phase angles. The color maps in the top panels represent the corresponding vorticity fields derived from the measured velocity fields. Courtesy of Dr. Ivan Lopez at the University of Santiago de Compostela for providing the three high-resolution figures in the top row, which are the same as those in Figs. 11 and 12 in Lopez et al. (2015). To be consistent with the coordinate system used in Lopez et al. (2015), y coordinate in this figure points vertically upward.

short.

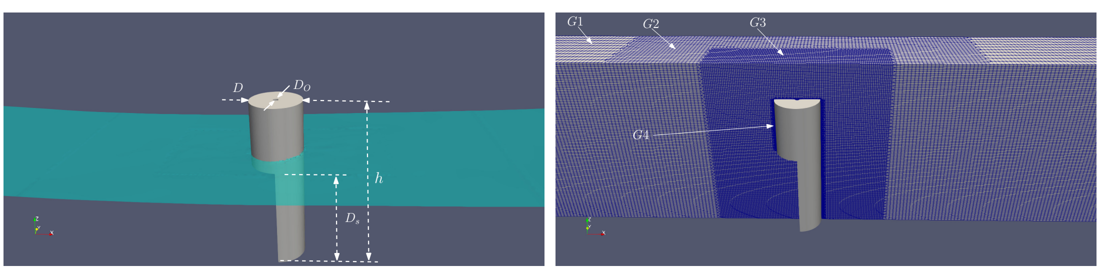

Fig. 5: Left: The bottom-sitting circular OWC-pile model; Right: the four nested local grids (G1 through G4) used to simulate the OWC-pile model.

A circular orifice is used to model a nonlinear PTO and its diameter D_o is 0.014 m. The OWC chamber is a partially submerged, forming an pneumatic chamber between the water surface and the top cover of the chamber. The overall height of the OWC pile h is 0.4 m, the height of the C-shaped support structure D_s is 0.25 m, the outer diameter of the pneumatic chamber D is 0.125 m, which results in a 1.25% opening ratio for the orifice used in this study. All walls of the OWC pile model have the same thickness of 0.003 m. Same as that used in the experiment of Xu et al. (2016), the water depth is fixed at $d = 0.29$ m in the simulation. In the experiment, both the air pressure and surface displacement inside the OWC chamber were measured: a pressure sensor was used to measure the air pressure and a wave gauge was placed on the down-wave and at 3.7 cm away from the axis of symmetry. The experimental data provided by the pressure sensor and the wave gauge are used for further model verification in this section.

The bottleneck in the numerical simulation of wave-interaction with the OWC pile is the high-speed air flow through the orifice, which requires a much finer grid and very small time step. Referring to the right panel of Fig. 5, four nested local grids are introduced in the vicinity of the OWC pile: grids G1, G2, G3 and G4. The information of these four grids are summarized in Table 2. The total number of mesh count is around 3 million.

All simulations were performed on Stampede2 at TACC using 160 cores. CFL numbers in the range of 0.4 and 0.6 were used in the simulations. About 30 wall-clock hours were typically needed to produce 20 s of real-time results. One wave condition is considered in this study: wave periods $T = 1.0$ and wave height $H = 0.04$ m.

3.1. Comparison with the experimental results of Xu et al. (2016)

The numerical model and setup for the OWC pile were further verified by comparing with one set of experimental results reported in Xu et al. (2016). Fig. 6 show comparisons between the measured and simulated pressures and surface elevations. It can be seen that both the surface displacement and the air pressure inside the pneumatic chamber can be captured well by the numerical model and grids, suggesting that the numerical model and setup, especially the grids used to simulate the air flow through the orifice, are suitable.

3.2. Oscillating motion of the water column inside the pneumatic chamber

For the purpose of later discussion, the oscillation of the water column is represented by the mean motion of the water surface inside the OWC chamber, $\bar{\eta}(t)$, obtained by

$$\bar{\eta}(t) = \int_S \eta(x, y, t) dx dy \tag{13}$$

Table 2: Information of the grids for the circular OWC model

size/zone	G1	G2	G3	G4
Δx (m)	0.01	0.01	0.005	0.0025
Δy (m)	0.025	0.0125	0.006	0.003
Δz (m)	0.005	0.005	0.0025	0.00125

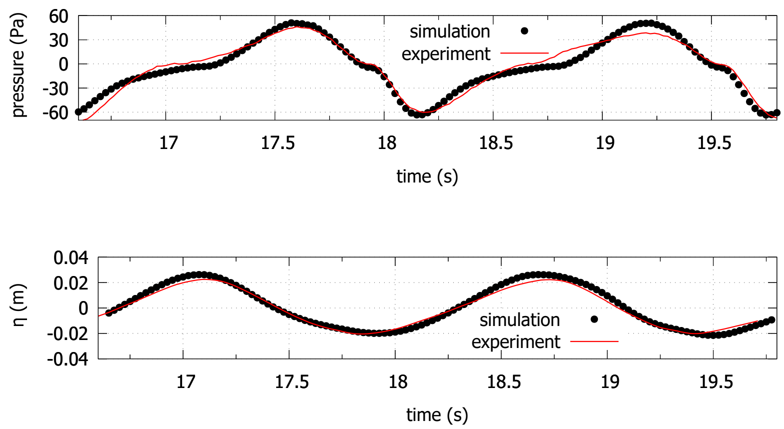

Fig. 6: Measured and simulated pressures and surface elevations. Top panel: pressure inside the OWC chamber; bottom: surface elevation measured inside the OWC chamber. Wave period=1.6 s and wave height=0.04 m.

where S and $\eta(x, y, t)$ are, respectively, the cross-sectional area of and the surface displacement inside the OWC chamber. The surface displacement measured at 1 cm away from the surface of the OWC pile and in the vertical plane of symmetry, the cross-sectional mean surface displacement $\bar{\eta}(t)$ (or "average surface displacement" for short), the surface displacement at the center of the OWC chamber are shown in Fig. 7. It can be seen that there is a slight difference between the average surface displacement and the displacement at the center due to the non-uniformity of the water surface inside the OWC chamber (Xu and Huang, 2019). Fig. 7) also include the surface displacement 5 mm away from the OWC chamber on the up-wave side in the vertical plane of the symmetry (referred to as "front" and the surface displacement 1 cm away from the OWC chamber on the down-wave side 45 degrees to the vertical plane of symmetry (referred to as "45° downwave"). The displacement at 45° downwave closely follows the average displacement; but there is a phase difference between the surface displacements in front of and that inside the OWC chamber.

As far as the oscillating water column is concerned, there are two stages: (1) the inhalation stage in which the average surface displacement rises and the pneumatic chamber contracts, causing the air to flow out of the pneumatic chamber stage in which the average surface displacement falls and the pneumatic chamber expands, causing the air to flow into the pneumatic chamber through the orifice. Referring to Fig.7, the inhalation process begins at the phase "o", through the phases "a", "b", "c" and "d", and ends at the phase "m"; the exhalation process begins at the phase "m", through the phases "e", "f","g" and "h", and ends at the phase "q". Between phases "a" through "d", the elevation of the water surface just in front of the OWC chamber is higher than that of the average water surface inside the chamber, causing the water to flow into the OWC chamber. At phase "d", the water surfaces on the two sides of the skirt have about the same elevation, and the continued rise of the average water surface between the phase “d” and the phase “m” is purely due to the kinetic energy in the water column inside the chamber. At the phases “e”, “f”, and “g”, the elevation of the average water surface inside the OWC chamber is higher than that just in front of the OWC chamber, causing the water to flow out of the chamber. There is a phase between the phases “g” and “h” at which the water surfaces on the two sides of the skirt have the same elevation, and the continued fall of the average water surface between this phase and the phase “h”, again, is due to the kinetic energy in the water column inside the chamber.

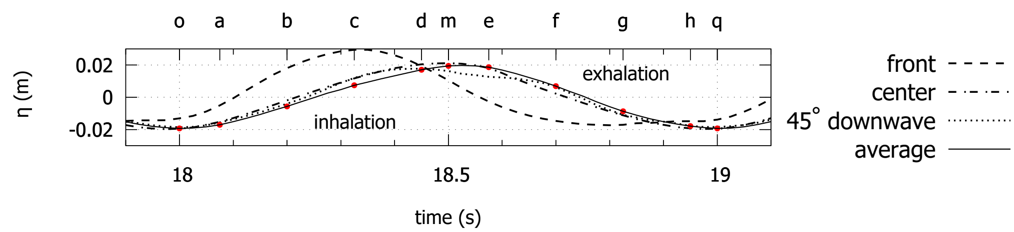

Fig. 7: Time series of surface displacements at three locations and the cross-sectional mean surface displacement inside the pneumatic chamber with PTO. Wave period=1.0 s.

The oscillating motion of the water column inside the OWC chamber affects the flow around the OWC pile.

3.3. Time series of horizontal velocity at selected locations

There are several physical processes involved in this problem, including wave scattering, wave radiation, vortex formation and shedding, as well as the transport, diffusion and dissipation of vorticity. The wave scattering and radiation processes can be stabilized quickly. One vortex is shed for the lower tip of skirt of the OWC chamber and the two vertical edges of the C-shaped structure during each half period. It may take more than 15 wave periods for the vortex shed from the lower tip of the skirt to reach the bed. A stabilized flow field is reached only when vorticity diffusion, transport and dissipation processes are stabilized. The vortices shed from different parts of the C-shaped structure may have slightly different frequencies; as a result of the interaction of these rotating flows, even a stabilized velocity field near the OWC pile model is reached, it can still be near-periodic in nature (Pier, 2013).

To verify that the velocity fields to be presented in the next section are stabilized results, we first examine time series of the magnitude and direction of the velocity in a horizontal plane. Fig. 8 shows the time series of the velocity magnitudes and directions at several chosen points: three points are on the horizontal plane located at 0.005 m above the bed and three points are on the horizontal plane located at 0.1 m above the bed. The locations of these points relative to the C-shaped structure are indicated by the letters “A”,“B” and “C” next to the C-shaped cross section. After 18 s, both the magnitudes and directions of the velocity at the same location relative to the C-shaped cross-section but different elevations are similar, suggesting that the vorticity transport, diffusion and dissipation processes are stabilized.

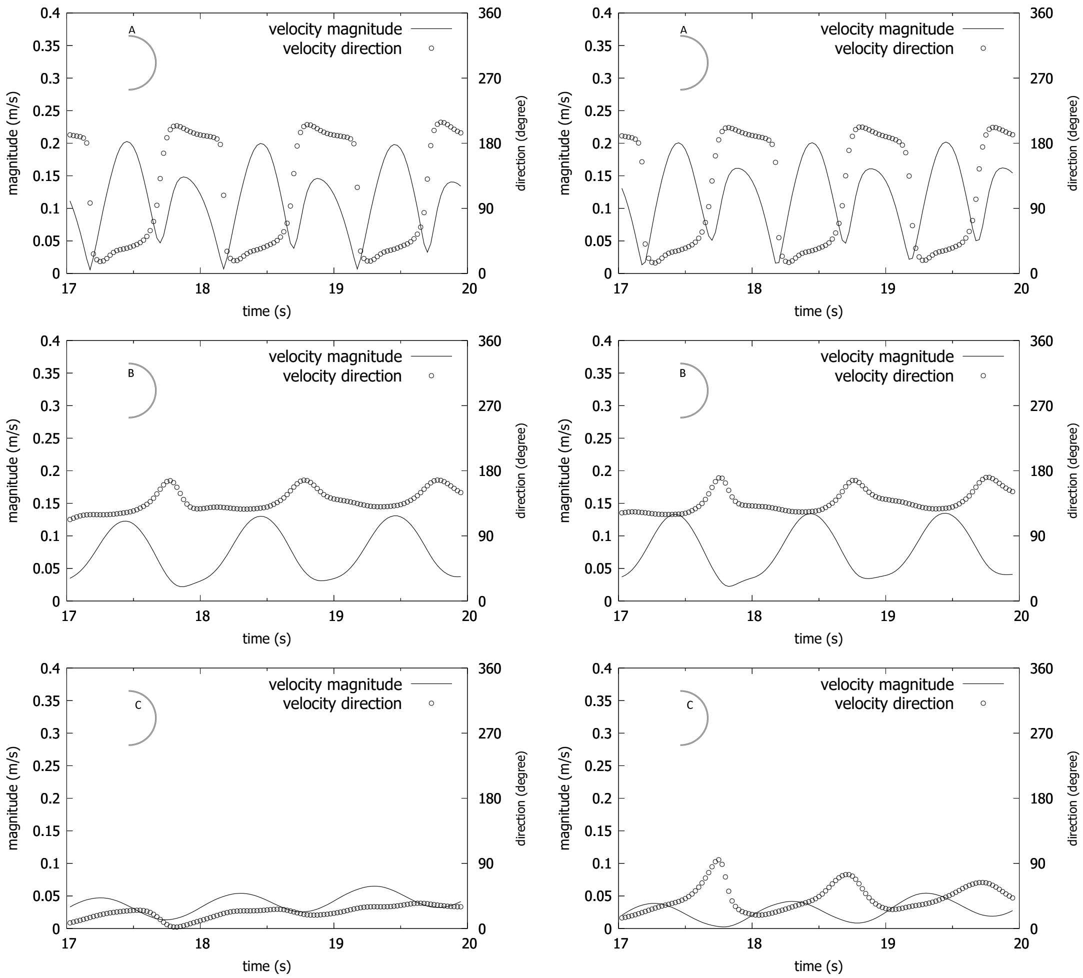

Fig. 8: Magnitude and direction of the velocity field in two horizontal planes at three representative points A, B and C. The coordinates of these three points are: point A is at (5,0.325), point B at (5,0.30), and pint C at (5.015,0.2688). The center is at (5,0.25). Left column: the horizontal plane is at 0.005 m above the bottom; right column: the horizontal plane is at 0.1 m above the bottom.

The stabilized velocity field may have a time-mean component. This can be learned from magnitude and direction of the time series of velocity at a point. Take the velocity field in a horizontal plane as example. In a horizontal plane, the two velocity components, after ignoring the higher order higher and lower harmonic components, can be approximated by

$$u = U + u_0 \cos(\omega t + \phi_u), \quad v = V + v_0 \cos(\omega t + \phi_v), \tag{14}$$

where the vector (U, V) is the velocity of the time-mean flow, the vector (u_0, v_0) is the amplitude vector of the oscillatory flow, and ϕ_u and ϕ_v are the phase angles of the corresponding fluctuation components which are not important in the following analysis. The velocity magnitude $|\vec{u}|(t)$ and direction $\theta(t)$ are defined by

$$
\begin{aligned}
|\vec{u}|(t) &= \sqrt{[U + u_0\cos(\omega t + \phi_u)]^2 + [V + v_0\cos(\omega t + \phi_v)]^2} \\
\tan\theta(t) &= \frac{V + v_0\cos(\omega t + \phi_v)}{U + u_0\cos(\omega t + \phi_u)}
\end{aligned}
\tag{15}
$$

The direction angle θ is relative to the positive x direction and increases anti-clockwise. If $v_0 \geq V$, $\theta(t)$ will contain instants of time at which $\theta = 0$; if $u_0 \geq U$, $\theta(t)$ will contain instants of time at which θ=90 or 270 degrees. If both $u_0 \gg U$ and $v_0 \gg V$, $|\vec{u}|$ will have two oscillations within one period of the fundamental waves. If the higher order fluctuations are included in Eq. (14), the conclusions drawn above still hold.

Referring to Fig. 8, the flows at these points are not pure sinusoidal, suggesting a strong influence of vortex shedding. At point "A" located at either 0.005 m or 0.1 m above the bed, $\theta(t)$ contains two instants of time at which θ=90 degrees and $|u|(t)$ oscillates twice within on period, suggesting that the time-mean velocity at this point is much weaker than the oscillatory velocity. At point "B", the velocity direction changes between 110 degrees and 170 degrees within one period and $|u|(t)$ oscillates only once within one wave period; therefore, the oscillatory flow is weaker than the time-mean flow at this point. At point "C", the velocity direction changes between 5 degrees and 35 degrees and $|u|(t)$ oscillates only once within one period; therefore, the oscillatory flow is weaker than the time-mean flow at this point.

Since the flow is near-periodic and has a time-mean component, a meaningful mean can be defined over a time scale longer than, say one wave period, to reduce possible uncertainty in the calculated time-mean velocity.

Results of the time-mean velocity fields in two horizontal planes are presented later in Sections 3.6 and 3.7, where the time-mean velocity fields are defined over two wave periods.

3.4. Flow around the circular surface of the OWC chamber

The KC number defined by the diameter of the OWC chamber D and the orbital velocity of the incident waves (ωA), i.e., $KC = 2\pi A/D$, is 1, and the frequency number, i.e., $\beta = D^2/(\nu T)$, is 1.56 $\times 10^4$ for wave period=1.0 s. For a circular cylinder of the same diameter in the same wave field, there is no flow separation from the cylinder surface for $KC < 3$ (Iwagaki and Ishida, 1976). By examining the simulated velocity field in a horizontal plane located at 0.01 m above the tip of the skirt, it is found that there is flow separation from the surface of the OWC-chamber section.

3.5. Vortices shed from the lower tip of the skirt

One way to show the vortices shed from the lower tip of the skirt is the velocity field in the vertical plane of symmetry. Fig. 9 shows eight snapshots of the velocity field in the vertical plane of symmetry and the corresponding phases at which these eight snapshots are taken. Since nested grids are used in the vicinity of the OPW pile, these velocity fields were prepared by using a uniform grid to interpolate the velocity fields on the original nested grids. The key features of the velocity field in the vertical plane of symmetry in both the inhalation and exhalation stages are similar to those for a rectangular 2D OWC integrated with a breakwater studied by Lopez et al. (2015), even through the OWC-pile structure considered here is 3D axis-symmetric. These key features are: (1) one vortex is shed from the lower tip into the OWC in inhalation stage, and (2) one vortex is shed from the lower tip out of the OWC chamber in the exhalation stage. The accompanying counter-rotating vortcies are not as obvious in both stages, possibly because the thickness of the shirt is much smaller than other dimensions of the OWC pile. It is interesting to note that in the exhalation stage the outflow comes out of the OWC chamber predominantly at an angle about 45 degrees to the horizontal. Because the vortcies shed from the lower tip of the skirt are not large enough to touch the bed and the accompanying counter-rotating vortcies are very weak, the vortices shedding at the lower tip are not expected to have a direct influence on the near-bed velocity field: possible influence on near-bed flow field is possible through the downward transport and diffusion of these vortices.

3.6. Vortices shed from the two sharp edges of the C-shaped structure

Around the C-shaped structure, the vortices shed from the two sharp edges can be described by the velocity fields in horizontal planes at different elevations.

Fig. 10 shows eights snapshots of the velocity fields in a horizontal surface located at 0.1 m above the bed, with the corresponding phases being marked on the plot of $\bar{\eta}(t)$ as "a" through "h". Four phases are in the inhalation stage and the other four in the exhalation stage. The wave period is 1.0 s. The velocity field of the time-mean flow is also included in Fig. 10.

The velocity field in this horizontal plane is approximately symmetric about the vertical plane of symmetry. This near-symmetric flow pattern might be lost in certain ranges of KC and Reynolds numbers (Tong et al., 2017), especially when the KC number is large. Unlike in the case of a circular cylinder in a steady current, there is no lee-wake vortex formed on the lee side of the OWC pile because the flow is oscillatory and the KC number defined by $KC = 2\pi A/D$ is just about 1, which is much less than the minimum value of 7 required for the formation of lee-wake vortex (Mei, 1992). Instead of lee-wake vortices, vortices are shed from the two sharp edges of the C-shaped support structure. The formation and shedding of these vortices are affected by both the incoming waves and the motion of the oscillating water column. On the convex side of the C-shaped structure, one vortex is formed at each sharp edge of the C-shaped structure and grow in size between phases "b" and "f". However, flow separation does not occur because of the small KC number: the vortices on the convex side gradually disappear from phases "g" to "a" due to transport, diffusion and dissipation. On the concave side of the C-shaped structure, a vortex is formed close to each edge in accompany with the vortex on the convex side ; therefore there are a pair of counter-rotating vortices on the concave side of the C-shaped structure. These two

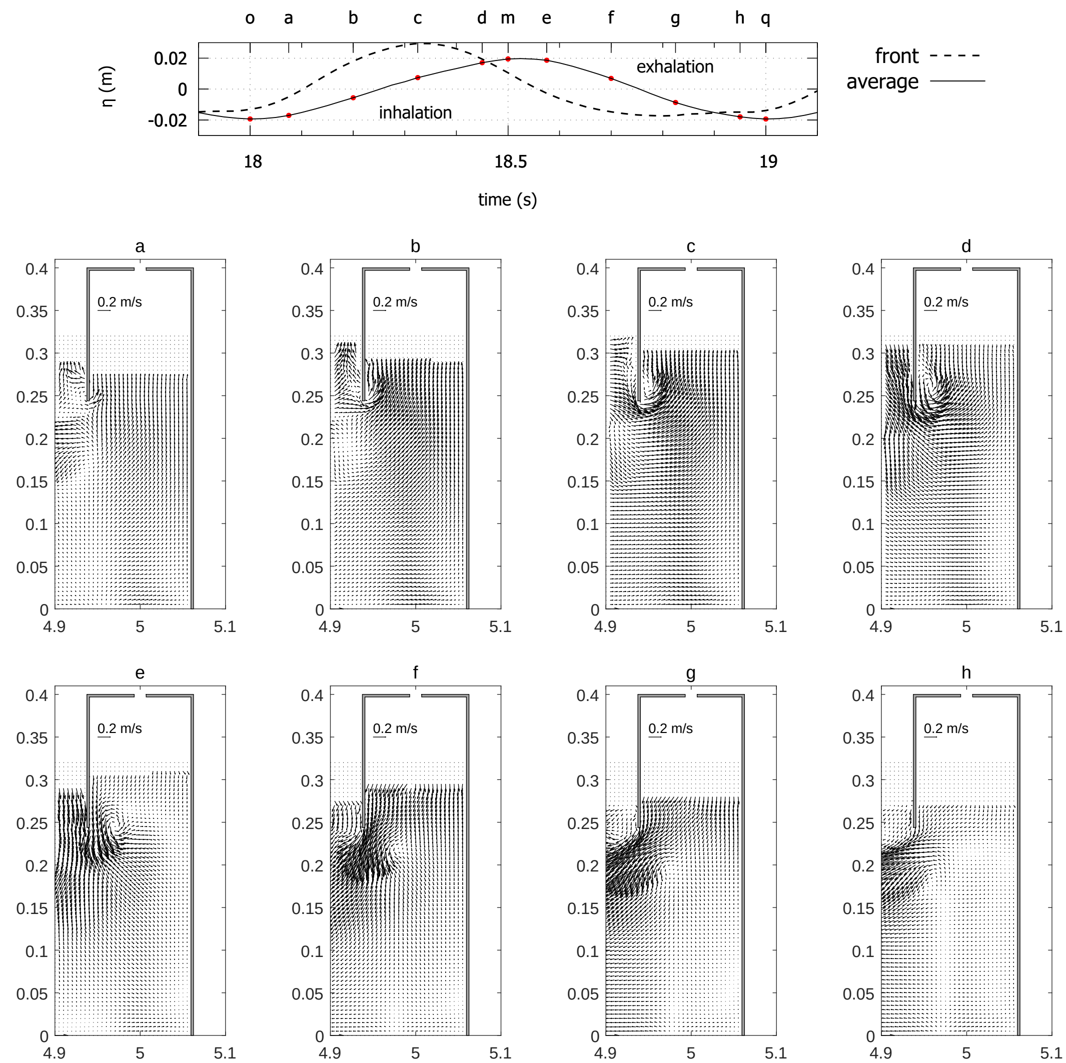

Fig. 9: Representative velocity fields in the vertical plane of symmetry: the top four panels are for the inhalation stage and the bottom for panels are for the exhalation. Wave period=1.0 s. Incident waves come from the left.

vortices are detached from the concave surface of the C-shaped structure and long-lasting, and there is no reversal of their directions of rotation during one wave period, indicating the existence of a time-mean flow field. The time-mean velocity field in the horizontal plane located at 0.1 m above the bed, obtained by averaging the velocity field over two wave periods, is shown in Fig. 10 as the last panel; the time-mean flow has a pair of counter-rotating vortices on the concave side of the C-shaped structure, with the maximum velocity being about 0.1 m/s.

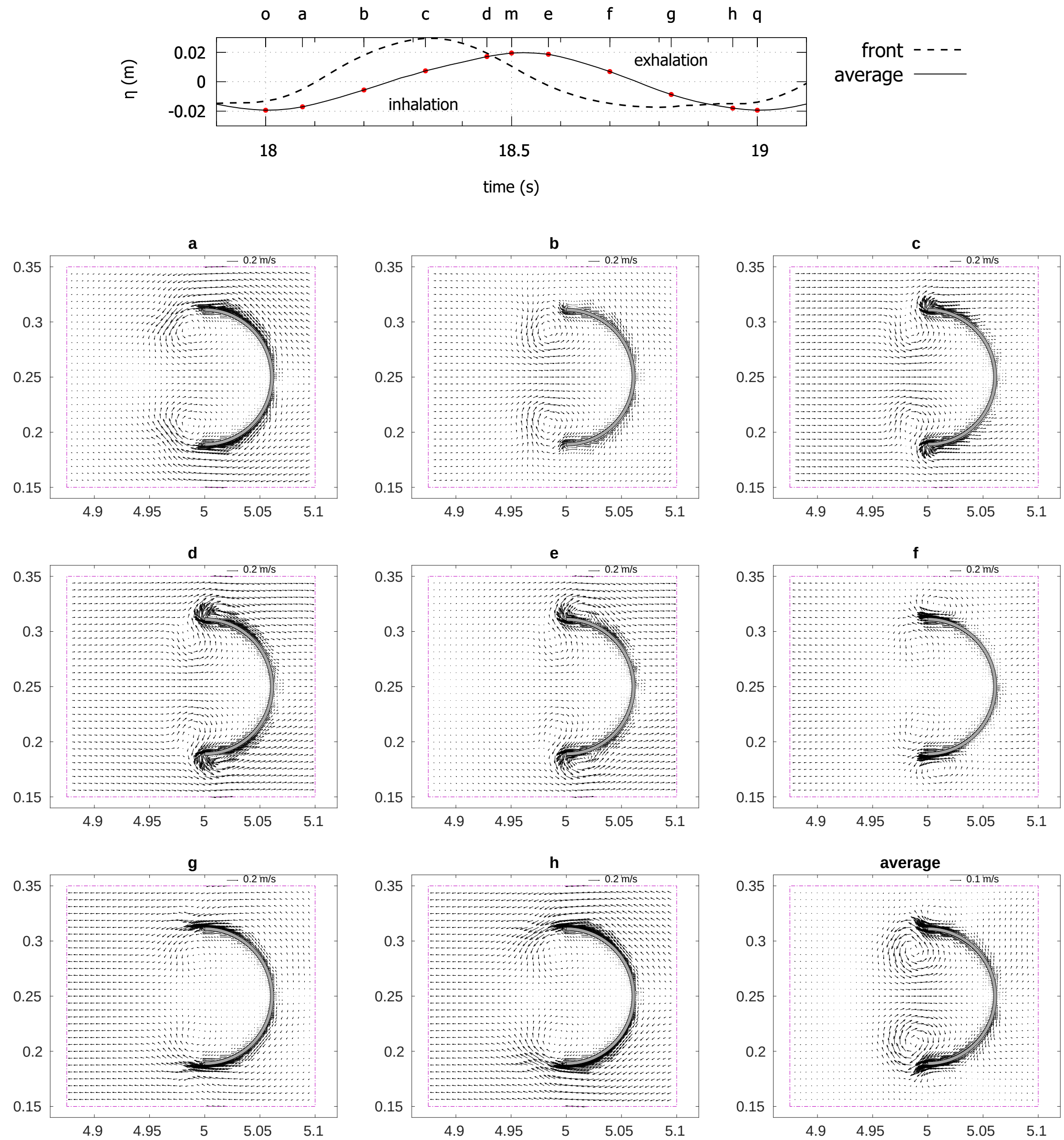

Fig. 10: Eight snapshots of the velocity field in a horizontal plane located at 0.1 m above the bed. The eight phases are indicated in the top panel. The last panel in the bottom row is the time-mean velocity field in the same horizontal plane. Incident waves come from the left.

3.7. Near-bed flow characteristics

For wave-induced sediment transport and local scour, the characteristics of the flow close to the bed are of interest. Fig. 11 shows eight snapshots of the velocity fields in a horizontal surface located at 0.005 m above the bed, with the corresponding phases being marked on the top panel. The wave period is 1.0 s. Comparing with Fig. 10, it can be concluded that both the instantaneous and time-mean velocity fields in horizontal planes at these two different elevations are similar, indicating that the vorticity transport, diffusion and dissipation have been stabilized. The time-mean flow has two counter-rotating vortices close to each edge of C-shaped structure, with the size of the vortex on the concave side being larger than that on the convex side. The maximum time-mean velocity is on the order of 0.1 m/s, which occurs in the vicinity of the two edges of the C-shaped structure. These time-mean flows may cause fine sand moving with them to leave the two edges and deposit in front of the C-shaped structure. It is remarked that both the instantaneous and time mean characteristics of the near-bed flow shown in Fig. 11 are important for understanding near-field sediment transport and local scour around the OWC pile.

3.8. Wave-induced morphological changes around an OWC pile

The instantaneous and time-mean flow patterns suggest that once sediment grains are mobilized (either rolling on the bed or suspended to a level close to the bed), deposition may be expected on the inner side of the C-shaped structure, close to the vertical plane of asymmetry, and erosion may be expected at two edges of the C-shaped structure. This has been confirmed qualitatively by the results of a wave-flume test reported in Zhang (2019), who experimentally measured wave-induced morphological change in the vicinity of a OWC-pile with slightly different dimensions. A summary of the wave-induced morphological changes in the vicinity of the OWC pile reported in Zhang (2019) is sketched in Fig. 12

A clear correlation between the flow pattern and the morphological change can be observed by comparing Fig. 11 and Fig. 12. The vortices on the convex side of the C-shaped structure are responsibly for the maximum erosion in the vicinity of the two edges; the time-mean flow seems to be responsible for the slight accretion on the concave side right in front of the C-shaped structure.

4. Discussion

For current-induced local scour around a vertical pile, the flow is obstructed by the pile, resulting in a stagnation line on the front side of the pier. As a result, the stagnation pressure causes a downward hydraulic gradient to develop in front of the pile, which drives a steady downflow directed towards the bed and forces the flow to circulate near the bed (Roulund et al., 2005). At the same time, the development of viscous boundary layer causes the flow to separate and shed vortices from the surface of the pile. The combination of the vortex shedding and the stagnation-caused downflow produces a vortex ring with its axis conform with the shape of the convex side of the pile, resulting in the so-called horseshoe vortices wrapping around the convex side of the base of the pile. Horseshoe vortices are responsible for the current-induced local scour at piles (Roulund et al., 2005; Akan, 2006). The sizes of the horseshoe vortcies around a vertical pile are usually small, confined to a narrow region close to the base of the pile.

Numerical results for an OWC pile in waves of wave period 1.0 s do not support the existence of a steady downflow along the front side of the C-shaped structure and

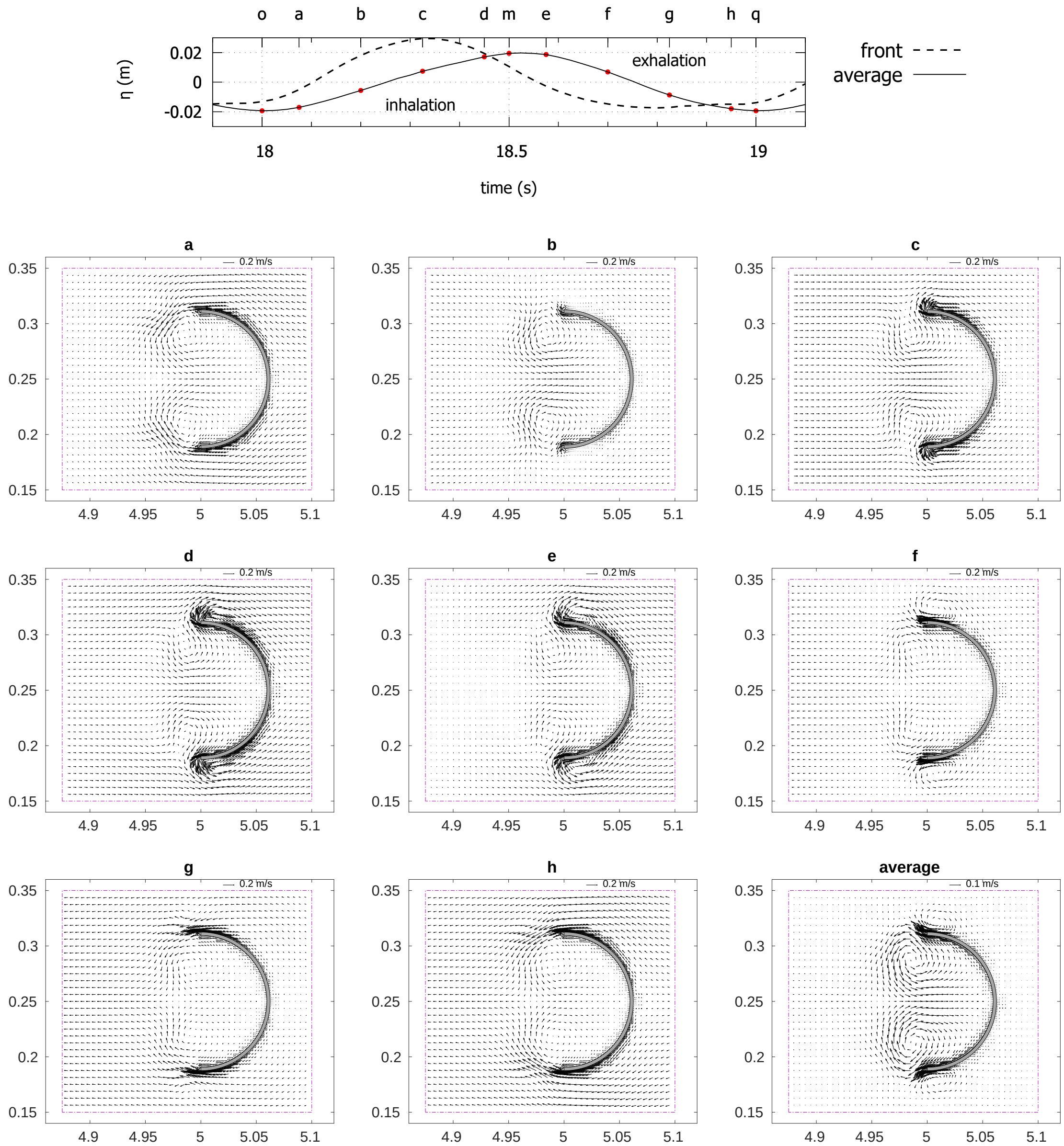

Fig. 11: Eight snapshots of the velocity field in a horizontal plane located at 0.005 m above the bed. The eight phases are indicated in the top panel. The last panel in the bottom row is the time-mean velocity field in the same horizontal plane. Wave period=1.0 s and the time range is 18 s to 19 s. Incident waves come from the left.

horse-shoe vortices on the concave side of the base of the C-shaped structure. This is possibly because of the following factors: (1) the geometric shape of an OWC pile is very different from that of a circular pile, which results in different wave scattering patterns. (2) the flow in the present problem is unsteady and spatially non-uniform; (3) there is a strong oscillatory motion of the water column inside the OWC chamber; and (4) the vortices shed into the interior of the C-shaped structure may strongly

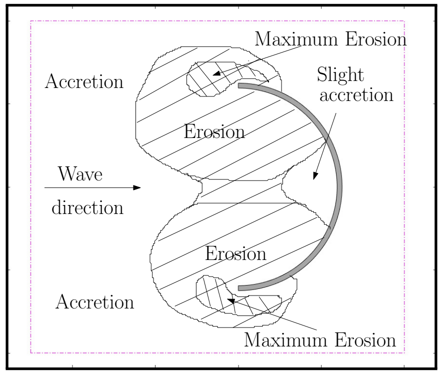

Fig. 12: A sketch of wave-induced morphological change in the vicinity of an OWC pile.

affect the local pressure distribution and thus local flow field.

Wave-induced streaming or wave-induced mass transport (Longuet-Higgins, 1953) is not a key flow characteristic for the present problem. Longuet-Higgins (1953) showed that wave-induced Eulerian streaming (or, wave-induced mass transport) as well as a steady vorticity exist inside the Stokes' boundary layer adjacent to the seabed. This mean vorticity may diffuse into the inviscid core region over a time scales several orders of magnitude longer than wave period. The ratio of the wave-induced streaming velocity to the wave orbital velocity is on the order of magnitude of the wave steepness. When a circular cylinder is placed vertically in regular waves, Lamoure and Mei (1977) found that due to wave-induced mass transport, fluid particles outside the wave boundary drift toward the convex side of and away from the convex side of the vertical cylinder, with the wave-induced mass transport in the vicinity of a structure being smaller than the wave orbital velocity by a factor scaled by the wave steepness. For the present problem, the wave-induced mass transport velocity should be on the order of 0.01 m/s, but the time-mean velocity found here is relatively strong, on the order of 0.1 m/s. The time required for the wave-induced streaming reach to an elevation d from the bed is about d^2/ν; it needs at least 25 s to reach the level d =0.005 m, and at least 10^4 s to reach to the level $d = 0.1$ m. However, the time-mean velocity field found here exists well before 20 s. Furthermore, the time-mean velocities are vertically similar at elevations 0.005 m and 0.1 m above the bed, excluding the effect of vorticity diffusion from the bed into the core region. Therefore, it is concluded that the mean velocity fields at elevations 0.005 m above the bed are not affected by the wave-induced streaming in any significant way.

Hongji instability (Honji, 1981) is not a flow phenomena in the present problem. For a circular cylinder in a spatial-uniform, oscillatory flows at low KC numbers (KC<15), it has been known that mushroom-like flow structures exist around the cylinder due to Hongji instability. Hongji instability appears during the transition from two dimensional laminar flow to turbulent flow in a certain range of frequency number (<160) defined by the ratio of the Reynolds number and the KC number (An et al., 2011; Zhao et al., 2011). Shao et al. (2016) studied a L-shaped structure and Tong et al. (2017) studied a square cylinder in spatially-uniform, oscillatory flows at KC numbers and the frequency numbers similar to those examined in An et al. (2011); both did not report Hongjin instability, possibly because of the lack of the transition from two-dimensional laminar flow to turbulent flow due to the sharp edges in the structures. The OWC pile studied here has sharp edges at the lower tip of the skirt and the two ends of the C-shaped support structure, and the unsteady flow is three dimensional; therefore, mushroom-like streaks around the structure due to Hongji instability are not expected.

5. Conclusions

A circular OWC supported by a bottom-sitting C-shaped structure (an OWC pile) was studied using two-phase flow numerical simulations. The validation and verification of the numerical model and the numerical setup were done by comparing with the measured surface elevations, air pressure inside the pneumatic chamber and instantaneous velocity fields reported by two published papers. Vortices are shed from both the lower tip of the skirt of the OWC chamber and the two edges of the C-shaped support structure, with the vortices on the convex side of the C-shaped structure being smaller, stronger and short-lived and the vortices on the concave side of the C-shaped structure being larger, weaker and long-lived. These vortices result in a time-mean velocity field around the OWC pile, with two large counter-rotating vortices on the concave side of the C-shaped structure. No horseshoe vortices are found in the simulated velocity field. The morphological changes around the OWC pile is strongly correlated to the vortices shed from the two edges of the C-shaped structure.

6. Acknowledgement

Dr. Ying Min Low at the National University of Singapore is acknowledged for supporting this work by supervising a Master's project on a wave-flume study of wave-induced scour at an OWC pile. The authors thank Dr. Ivan Lopez at the University of Santiago de Compostela for providing us with a set of high resolution figures of his PIV measurement results.This work was supported by the US National Science Foundation under grant number CBET-1706938 and the Extreme Science and Engineering Discovery Environment (XSEDE) under grant numbers OCE170015 and ENG180008. XSEDE is supported by National Science Foundation grant number ACI-1548562. Any opinions, findings, and conclusions or recommendations expressed in this material are those of the author(s) and do not necessarily reflect the views of the National Science Foundation. This is SOEST contribution No. 11777.

Appendix A. Wave generation and wave absorption methods

Waves are generated by specifying the velocity field according to a chosen wave theory and the phase fraction field on the inlet boundary at each time step. As second-order Stokes wave theory is employed here, the velocity profile on the inlet boundary $x = 0$ is specified by the two velocity components in the x and y directions.

$$u_x = \frac{\pi H}{T}\frac{\cosh k(z+d)}{\sinh kd}\cos(kx-\omega t+\phi) + \frac{3}{4}\frac{\pi H}{T}\frac{\pi H}{L}\frac{\cosh 2k(z+d)}{\sinh^4 kd}\cos 2(kx-\omega t+\phi), \quad (A.1)$$

$$u_y = \frac{\pi H}{T}\frac{\sinh k(z+d)}{\sinh kd}\sin(kx-\omega t+\phi) + \frac{3}{4}\frac{\pi H}{T}\frac{\pi H}{L}\frac{\sinh 2k(z+d)}{\sinh^4 kd}\sin 2(kx-\omega t+\phi), \quad (A.2)$$

and the corresponding free surface elevation η is

$$\eta = \frac{H}{2}\cos(kx-\omega t+\phi) + \frac{\pi H^2}{4L}(1+\frac{3}{2\sinh^2 kd})\coth\ kd\cos 2(kx-\omega t+\phi), \quad (A.3)$$

where u_x and u_y are the velocity components in x and y directions respectively. H = wave height, k = wave number, ω = wave angular frequency, t = time, L = wavelength, d water depth. The shift angle ϕ is set to be 0 in this study.

In the wave absorbing section, a source term S_m is added to the momentum equation:

$$\frac{d\rho U}{dt} = \rho F + P + S_m \quad (A.4)$$

where F is the mass force per volume unit, P is pressure force and S_m is a sink term calculated by

$$S_m = -\mu DU \quad (A.5)$$

where D is the so-called Darcy coefficient to be specified by the user. The wave absorption performance is determined by wavelength, the value of D and the length of the absorption section. Based on numerical test results, a value of $D = 5 \times 10^5$ was selected in this study. With D being determined, the necessary length of absorbing section was carefully selected to make sure the wave energy at the end of the flume is almost zero. To reduce the total mesh count, the mesh is coarsened gradually in x direction from $\Delta x = 0.02m$ at the front side of the wave absorbing section to $\Delta x = 0.12m$ at the rear side of the wave absorbing section.

References

Akan, A. O., 2006. Open Channel Hydraulics. Butterworth-Heinemann.

An, H., Cheng, L., Zhao, M., 01 2011. Direct numerical simulation of oscillatory flow around a circular cylinder at low keulegancarpenter number. Journal of Fluid Mechanics 666.

Ashlin, S. J., Sannasiraj, S., Sundar, V., 2015. Wave forces on an oscillating water column device. Procedia Engineering 116, 1019–1026.

Breusers, H., Nicollet, G., Shen, H., 1977. Local scour around cylindrical piers. Journal of Hydraulic Research 15 (3), 211–252.

Bureau of Ocean Energy Management, 2017. Ocean Wave Energy. http://www.boem.gov/Renewable-Energy-Program/Renewable-Energy-Guide/Ocean-Wave-Energy.aspx, accessed: 2017-07-07.

Chiew, Y., Melville, B., 1987. Local scour around bridge piers. Journal of Hydraulic Research 25 (1), 15–26.

Deng, Z., Huang, Z., Law, A. W., 2013. Wave power extraction by an axisymmetric oscillating-water-column converter supported by a coaxial tube-sector-shaped structure. Applied Ocean Research 42, 114 – 123.

Elhanafi, A., 2016. Prediction of regular wave loads on a fixed offshore oscillating water column-wave energy converter using CFD. Journal of Ocean Engineering and Science 1, 268–283.

Hawaii State Energy Office, 2007. State of Hawaii Energy Policy Directives. http://energy.hawaii.gov/energypolicy, accessed: 2017-07-07.

Honji, H., 1981. Streaked flow around an oscillating circular cylinder. Journal of Fluid Mechanics 107, 509–520.

Huang, Z., Xu, C., Huang, S., 2019. A CFD simulation of wave loads on a pile-type oscillating-water-column device. Applied Ocean Research 31 (1), 41–49.

Iwagaki, Y., Ishida, H., 1976. Flow separation, wake vortices and pressure distribution around a circular cylinder under oscillatory waves. In: Proceedings of 15th Conference on Coastal Engineering. Vol. 3. ASCE, pp. 2341–2356.

Jacobsen, N. G., Fuhrman, D. R., Fredsöe, J., 2012. A wave generation toolbox for the open-source CFD library: OpenFoam?? International Journal for Numerical Methods in Fluids 70 (9), 1073–1088.

Jakobsen, M. M., Beatty, S., Iglesias, G., Kramer, M., 2016. Characterization of loads on a hemispherical point absorber wave energy converter. International Journal of Marine Energy 13, 1–15.

Kobayashi, T., Oda, K., 1994. Experimental study on developing process of local scour around a vertical cylinder. Coastal Engineering Proceedings 1 (24).

Lamoure, J., Mei, C. C., 1977. Effects of horizontally two-dimensional bodies on the mass transport near the sea bottom. Journal of Fluid Mechanics 83, 415–431.

Longuet-Higgins, M. S., 1953. Mass transport in water waves. Philosophical Transactions of the Royal Society of London. Series A, Mathematical and Physical Sciences 245, 535–581.

Lopez, I., Castro, A., Iglesias, G., 2015. Hydrodynamic performance of an oscillating water column wave energy converter by means of particle imaging velocimetry. Energy 83, 89 – 103.

Manes, C., Brocchini, M., 2015. Local scour around structures and the phenomenology of turbulence. Journal of Fluid Mechanics 779, 309–324.

Mattioli, M., Alsina, J. M., Mancinelli, A., Miozzi, M., Brocchini, M., 2012. Experimental investigation of the nearbed dynamics around a submarine pipeline laying on different types of seabed: the interaction between turbulent structures and particles. Advances in Water Resources 48, 31–46.

Mayer, S., Madsen, P. A., 2000. Simulation of Breaking Waves in the Surf Zone using a Navier-Stokes Solver. Proceeding to Coastal Engineering Conference I, 928–941.

Mei, C. C., 1992. The Applied Dynamics of Ocean Surface Waves. World Scientific.

Pier, B., 2013. Periodic and quasiperiodic vortex shedding in the wake of a rotating sphere. Journal of Fluids and Structures 41 (SI), 43–50.

Roulund, A., Sumer, B. M., Fredsøe, J., Michelsen, J., 2005. Numerical and experimental investigation of flow and scour around a circular pile. Journal of Fluid Mechanics 534, 351–401.

Rusche, H., 2003. Computational fluid dynamics of dispersed two-phase flows at high phase fractions. Ph.D. thesis, Imperial College London (University of London).

Shao, X., Zhang, X., Yu, Z., Lin, J., 2016. Numerical studies on the dynamics of an open triangle in a vertically oscillatory flow. Journal of Fluid Mechanics 788, 381–406.

Sheppard, D. M., Odeh, M., Glasser, T., 2004. Large scale clear-water local pier scour experiments. Journal of Hydraulic Engineering 130 (10), 957–963.

Sjkvist, L., Wu, J., Ransley, E., Engstrm, J., Eriksson, M., Gteman, M., 2017. Numerical models for the motion and forces of point-absorbing wave energy converters in extreme waves. Ocean Engineering 145, 1 – 14.

Sumer, B., Christiansen, N., Fredsøe, J., et al., 1992a. Time scale of scour around a vertical pile. In: The Second International Offshore and Polar Engineering Conference. No. 3. International Society of Offshore and Polar Engineers, pp. 308–315.

Sumer, B., Fredsøe, J., 1998. Wave scour around group of vertical piles. Journal of Waterway, Port, Coastal, and Ocean Engineering 124 (5), 248–256.

Sumer, B. M., Fredsøe, J., 1997. Scour at the head of a vertical-wall breakwater. Coastal Engineering 29 (3-4), 201–230.

Sumer, B. M., Fredsøe, J., Christiansen, N., 1992b. Scour around vertical pile in waves. Journal of Waterway, Port, Coastal, and ocean Engineering 118 (1), 15–31.

Tom, N. M., Madhi, F., Yeung, R. W., 2019. Power-to-load balancing for heaving asymmetric wave-energy converters with nonideal power take-off. Renewable Energy 131, 1208 – 1225.

Tong, F., Cheng, L., Xiong, C., Draper, S., An, H., Lou, X., 2017. Flow regimes for a square cross-section cylinder in oscillatory flow. Journal of Fluid Mechanics 813, 85–109.

Weller, H., Tabor, G., Jasak, H.and Fureby, C., 1998. A tensorial approach to computational continuum mechanics using object-oriented techniques. Computers in Physics 12, 620 – 1631.

Wilcox, D. C., 1993. Turbulence modeling for CFD. Vol. 2. DCW industries La Canada, CA.

Wilcox, D. C., 2008. Formulation of the kw turbulence model revisited. AIAA Journal 46 (11), 2823–2838.

Xu, C., Huang, Z., 2018. A dual-functional wave-power plant for wave-energy extraction and shore protection: A wave-flume study. Applied Energy 229, 963 – 976.

Xu, C., Huang, Z., 2019. Three-dimensional cfd simulation of a circular owc with a nonlinear power-takeoff: Model validation and a discussion on resonant sloshing inside the pneumatic chamber. Ocean Engineering 176, 184 – 198.

Xu, C., Huang, Z., Deng, Z., 2016. Experimental and theoretical study of a cylindrical oscillating water column device with a quadratic power take-off model. Applied Ocean Research 57, 19 – 29.

Xu, C., Huang, Z., Yao, Y., 2019. A wave-flume study of scour at a pile breakwater: Solitary waves. Applied Ocean Research 82, 89–108.

Zhang, Z., 2019. A wave flume study of scour at owc breakwater. Master's thesis, School of Civil and Environmental Engineering, National University of Singapore.

Zhao, M., Cheng, L., Zhou, T., 2011. Three-dimensional numerical simulation of oscillatory flow around a circular cylinder at right and oblique attacks. Ocean Engineering 38 (17), 2056 – 2069.